Fragment excitation energies at freeze-out in ^{84}Kr+^{93}Nb collisions at 45 MeV/nucleon

P. Staszel*
H. Niewodniczański Institute of Nuclear Physics, ul. Radzikowskiego 152, PL-31-342 Kraków, Poland

Z. Majka
M. Smoluchowski Institute of Physics, Jagellonian University, ul. Reymonta 4, PL-30-059 Kraków, Poland

L. G. Sobotka, D. G. Sarantites, and R. J. Charity
Department of Chemistry, Washington University, St. Louis, Missouri 63130

J. Cibor,† K. Hagel, N. Marie,‡ J. B. Natowitz, and R. Wada
Cyclotron Institute, Texas A&M University, College Station, Texas 77843

D. W. Stracener
Oak Ridge National Laboratory, Oak Ridge, Tennessee 37830

G. Auger, Y. Schutz, and J. P. Wieleczko
GANIL, Bôite Postale 5027, F-14021 Caen Cedex, France

R. Dayras
Service de Physique Nucléaire-Basse Energy, F-91191 Gif-sur-Yvette Cedex, France

E. Plagnol
Institut de Physique Nucléaire, IN2P3-CNRS, F-91406 Orsay Cedex, France

J. Barreto
Instituto de Física da UFRJ-CP21945-RJ, Brazil

E. Norbeck
Department of Physics, University of Iowa, Iowa City, Iowa 52242

(Received 22 December 1999; revised manuscript received 27 October 2000; published 23 May 2001)

The emission of light charged particles and intermediate-mass fragments (IMF's) from central collisions of 45 MeV/nucleon ^{84}Kr with ^{93}Nb has been studied. Violent collisions have been selected using the total collected charge condition. The analysis of the primary IMF excitation energies has been performed for four bins of the detected IMF charge ($2<Z_{\mathrm{IMF}}<20$). We find evidence that (a) the mean excitation energy per nucleon for these fragments is independent of fragment charge and approximately equal to 2.5 MeV, (b) the primary fragments at freeze-out preserve the entrance channel (combined system) N/Z ratio, and (c) the freeze-out volume itself is far from spherical.

DOI: 10.1103/PhysRevC.63.064610 PACS number(s): 25.70.Pq, 24.10.Pa

I. INTRODUCTION

One of the primary motivations for studying collisions between heavy nuclei far above the Coulomb barrier is to learn about the properties of nuclear matter at densities and temperatures far different from those encountered in nuclei at or near their ground states. This is related to the physics contained in the equation of state for infinite nuclear matter. However, the relationship between experimental data and bulk properties of strongly interacting matter is far from simple. The predominant decay mode of highly excited nuclei is the disassembly into several fragments [1]. The understanding of this multifragmentation phenomenon is difficult because the detected fragments are the cold remnants of the initially hot system.

A few studies have claimed that bulk volume expansion is needed in order to explain the production of intermediate-mass fragments in heavy-ion collisions [2,3]. If this is so, the collisions would be providing a means of studying the decay of subsaturation density nuclear systems. However, in order to have confidence that this scenario is correct, the dynamics must be well understood as well as how these dynamics are reflected in the few selected observables that are used in comparison with theory.

*Present address: Niels Bohr Institute, DK-2100 Copenhagen, Denmark.

†Present address: H. Niewodniczański Institute of Nuclear Physics, ul. Radzikowskiego 152, PL-31-342 Kraków, Poland.

‡Present address: Laboratoire de Physique Corpusculaire, ISMRA 6, Boulevard du Marechal Juin, F-14050 Caen Cedex, France.

The importance of dynamics has been made clear in investigations of observables that might be related to the temperature of the system. These observables include the slopes of light-particle kinetic energy spectra [4], relative population of excited states [5], and double yield ratios of neighboring isotopes [6–11]. The striking disagreement [12–14] of the extracted temperatures measured by these techniques suggests that these thermometers are sensitive to the thermalized energy at different epochs in the evolution of the nuclear system.

In the framework of the currently accepted scenario for the multifragmentation process, the compressed equilibrated hot system (created in the violent heavy-ion collision) first expands and emits mainly light particles. When the system reaches a sufficiently low density, the remainder disintegrates. The time at which this latter process occurs is called ''freeze-out.'' In this paper we use correlation techniques to extract information on the excitation energy per nucleon of intermediate mass fragments at or near freeze-out in central collisions between ^{84}Kr+^{93}Nb at 45 MeV/nucleon.

II. EXPERIMENT

A. Experimental setup

This experiment was performed at the GANIL facility using the Washington University Dwarf Ball/Wall multidetector system. A beam of 45 MeV/nucleon ^{84}Kr was used to bombard targets of ^{12}C, ^{27}Al, ^{45}Sc, ^{93}Nb, and ^{159}Tb. This work focuses on the nearly symmetric system ^{84}Kr+^{93}Nb. The center of mass (c.m.) energy for this system is 2.0 GeV. The Dwarf Ball/Wall detector system is described in detail in the literature [15] so only a few points will be made here. This 104-element, fast plastic-CsI(Tl) phoswich array covers laboratory angles from 6° to 35° with the Dwarf Wall (DW) and from 35° to 168° with the Dwarf Ball (DB). Light charged particles (LCP's=*p*, *d*, *t*, ^{3}He, and α particles) are identified using the pulse shape characteristics of the CsI(Tl) light output. The atomic numbers of intermediate-mass fragments (IMF's) ($2<Z_{\rm IMF}<20$) are determined by comparing the integrated fast light output from the plastic foils to the much slower light output produced by the CsI(Tl). The plastic foils vary in thickness from 200 to 20 μm for forward to backward angles, respectively. The IMF masses that are necessary in our analysis were assigned for β-stable nuclei. In this experiment, the energy calibration of the LCP was obtained from the punch-through points of the light ions. In other experiments, it has been verified that these points agree with those determined from inelastic scattering. The energy calibration for the heavy ions was done by the procedure described in Ref. [15]. This procedure makes use of a measured average response (of Dwarf Ball/Wall detectors) for heavy ions relative to that for LCP's. The detector system subtends approximately 88% of 4π with energy thresholds that vary with angle and ion charge. The thresholds for protons and α particles are 4 and 2 MeV/nucleon, respectively, for a large angular region (from $\approx$167° to near 35°). The energy thresholds increase at more forward angles. For protons, which is the worst case, the threshold increases by a factor of 2 at the most forward angles. The laboratory angular granularities are $\pm$14° for DB and $\pm$5° for DW in both polar and azimuthal directions. Some of the details of this experimental, including the overall multiplicity distributions, have been presented previously [16].

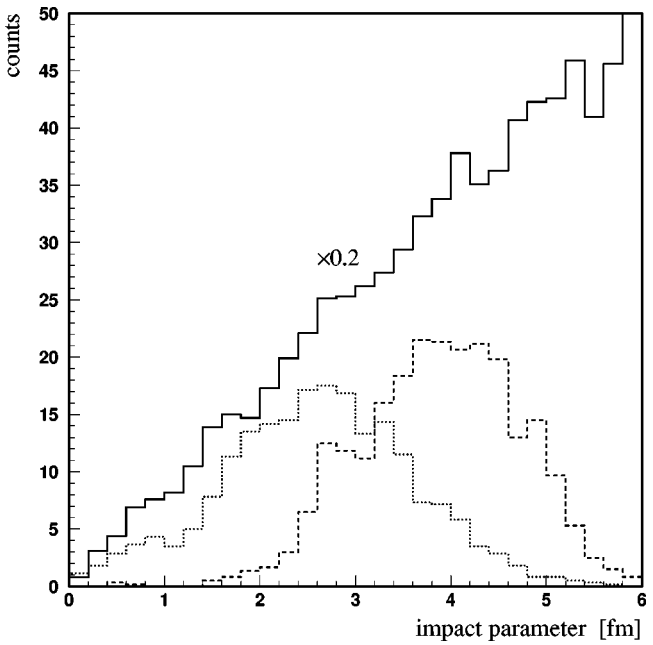

FIG. 1. Impact parameter distributions for a CHIMERA+GEMINI calculation when the total charge detected is greater than 60% of $Z_{\rm tot}$ (dashed-line histogram) and when the total charge detected in the DB is greater than 25% of $Z_{\rm tot}$ (dotted-line histogram). The solid-line histogram shows the results without any restriction given on the filtered events.

B. Selection of the violent collisions events

In Ref. [16], some results for the 45 MeV/nucleon ^{84}Kr + ^{159}Tb reaction were presented. It was determined that the condition imposed by the total detected charge, $Z_{\rm det}>75\%$ of $Z_{\rm tot}$, selects events that are characterized by high LCP multiplicity. $Z_{\rm tot}$ is a sum of the projectile and target nuclear charges. The impact parameter and the energy dependence of observables in intermediate-energy heavy-ion reactions were also studied by Tsang *et al.* in Refs. [17,18].

For the present study of the reaction ^{84}Kr+^{93}Nb at 45 MeV/nucleon, the violent collisions have been selected in a fashion similar to that used in Ref. [16]. Our procedure is guided by the results of the computer code CHIMERA [19], which provides a more quantitative estimate of the impact parameter distribution for gates on the total detected charge. This code is based upon the molecular dynamics concept [20,21]. The output of the CHIMERA code at time $t=150$ fm/c has been taken as input for the statistical code GEMINI [22]. Coulomb trajectories are following during the deexcitation process. The results of the CHIMERA-GEMINI calculation have been filtered through the experimental conditions using software that simulates the main physical features of the detection system (e.g., the geometry and the energy thresholds of each detector). The solid line histogram in Fig. 1 shows the overall event distribution as a function of impact

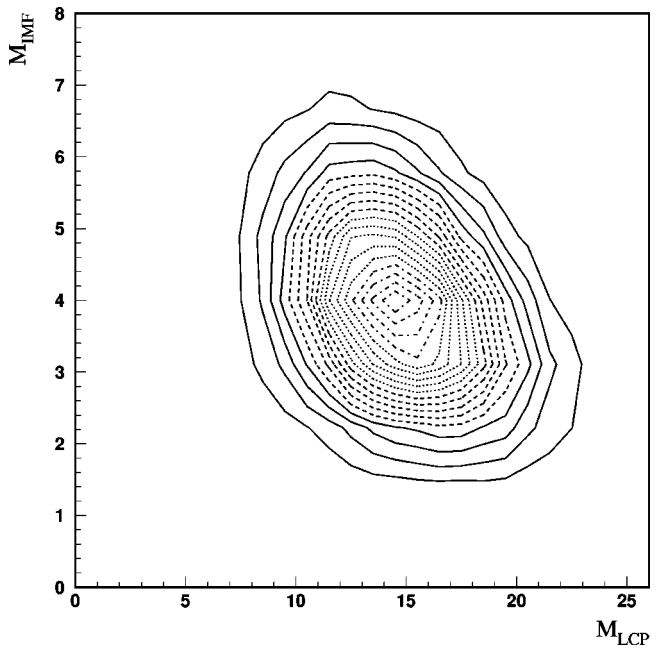

FIG. 2. Number of events (proportional to the area of the rectangle square's surface) as a function of the LCP multiplicity and IMF multiplicity when the collected charge in the DB detector was larger than 25% of Z_{tot}.

parameter generated by this simulation. This figure also displays the event distributions for (i) the condition that the total collected charge (detected in DW and DB) was larger than 60% of Z_{tot} (dashed line) and (ii) the condition that 25% of Z_{tot} is detected in the DB only (dotted line). One can see that the condition that requires substantial emission in the backward hemisphere (dotted line) significantly rejects peripheral collisions. Due to the improved rejection of peripheral collisions and our desire to focus on central collisions in the present work, condition (ii) has been used in this study.

Using this condition, the number of experimental events as a function of the LCP and IMF multiplicities is plotted in Fig. 2. This presentation of the charged particle multiplicity correlation is similar to that obtained in Ref. [16] [see Figs. 2(b) and 3(a) therein]. The average LCP and IMF multiplicities are about 14.5 and 4, respectively. Figure 2 shows the distinct correlation between the M_{LCP} and the M_{IMF}, which reflects the finite size of the disintegrating system, a point we made in our previous publication [16].

III. PROCEDURE OF THE PRIMARY FRAGMENT EXCITATION ENERGY RECONSTRUCTION

A. Overview

The primary fragment excitation energies can be determined from the multiplicities of associated LCP's evaporated from the IMF. However, the LCP's detected in coincidence with an IMF can originate from several sources, namely,

(1) the colliding system at the early phase of the reaction before thermal equilibrium is achieved,

(2) the composite excited system at freeze-out stage,

(3) the primary IMF of interest,

(4) all other primary IMF's.

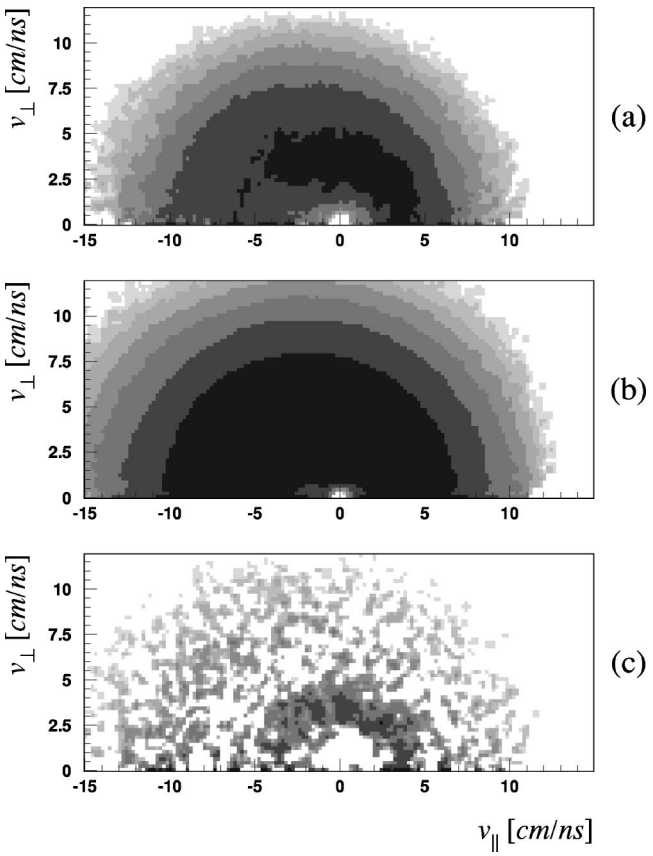

FIG. 3. Proton invariant velocity plot. The largest fragment in each event has been selected. (a) Raw coincidence, (b) background, and (c) difference [(a)−(b)].

The first and second of these sources produce LCP's that cannot be associated with any parent IMF, while the last produces LCP's not correlated to the IMF selected for study. Due to these background contributions, the LCP's from the second source cannot be associated with the selected residual IMF on an event by event basis. Nevertheless, some of the detected LCP's and IMF's are correlated via their common primary parent. If we calculate the relative velocities between the selected IMF and LCP's on an event by event basis, then the correlation should be seen as an excess of counts around the IMF position in a $v_{\parallel}$ versus $v_{\perp}$ representation. The velocities $v_{\parallel}$ and $v_{\perp}$ are the projections of the relative velocity into the IMF direction in the c.m. system and into a plane perpendicular to that axis, respectively. In this work, we assume that the average velocity of the detected fragment after statistical emission is equal to the velocity of the primary fragment.

Figure 3(a) displays the proton-invariant velocity plot in the reference frame described above and constructed for the largest fragment (IMF) detected in each event. One cannot see a substantial excess of protons around the point $v_{\parallel}=v_{\perp}=0$ cm/ns. This indicates that the correlated component represents a relatively small contribution to the total proton emission. In order to isolate uncorrelated emission, background plots have been constructed by replacing the relative velocity of LCP's that coincide with the given IMF by the relative velocity of the uncorrelated LCP's produced in a

different event. An example of the distribution for the uncorrelated component (from mixed events) is shown in Fig. 3(b). The result of the subtraction of this background from the total LCP emission is presented in Fig. 3(c). One can now clearly see correlated counts surrounding the IMF's position in velocity space. Similar pictures have been obtained for other combinations of the IMF's and LCP's. Such correlations have been exploited in previous work [23] to estimate the E^*/A for IMF's produced the ^{129}Xe+$^{\text{nat}}$Sn at $E/A = 50$ MeV reaction. Here, we have introduced a Monte Carlo simulation procedure to evaluate the freeze-out characteristics. This procedure that is described in the next section allows for the extraction of the excitation energies of the primary fragments.

B. Monte Carlo simulations

The simulations begin at the freeze-out time, at which it is assumed that the total excitation energy of the system is partitioned into three modes: (i) thermal motion of the point-like objects, (ii) radial expansion, and (iii) internal excitation of the fragments. At freeze-out, the relative distances between all fragments are such that mass exchange has ceased. The subsequent evolution of the system proceeds with the statistical decay of the excited IMF's with only the Coulomb repulsion operating between the fragments. The fragment decay times are drawn from the exponential distribution

$$P(t) \sim \exp\left(\frac{-t}{\tau}\right), \tag{1}$$

where τ is a free parameter characterizing the mean lifetime of the excited primary IMF's (see Sec. V and Fig. 17). Calculations are performed until the fragments become cold and the Coulomb accelerations become negligible. Finally, the generated events are presented to a software detector filter that simulates the experimental conditions.

C. Freeze-out stage characteristics

The freeze-out stage is characterized by the following.

(1) The freeze-out fragment partition, $\{Z_i, A_i\}$; $i = 1, \ldots, M_{\text{tot}}$, where M_{tot} is the total LCP and IMF multiplicity and $Z(i)$ and $A(i)$ are the charge and mass of the ith fragment, respectively.

(2) The freeze-out volume, V_{fo}, its shape, and the fragment distribution within that volume. Each fragment position is denoted by $\mathbf{r}_i$, with $i = 1, \ldots M_{\text{tot}}$.

(3) The initial fragment velocities, $\mathbf{v}_i$, $i = 1, \ldots, M_{\text{tot}}$.

Due to the limited detector acceptance the ''true'' asymptotic distributions are different from the experimental distributions. The ''true'' asymptotic distributions of the fragment charge, kinetic energy, and multiplicity, all of which have been obtained using an iterative tuning procedure, are presented in the next section.

For each event the desired asymptotic LCP multiplicity M_{LCP} and the IMF multiplicity M_{IMF} are chosen randomly from the two-dimensional asymptotic M_{LCP} versus M_{IMF} distribution. Such a selection ensures the correlation between the LCP and IMF multiplicities and the total multiplicity

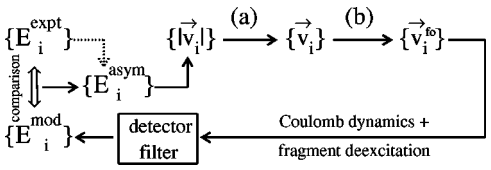

FIG. 4. Technique for determining the fragment velocities at freeze-out.

seen in the data; see Fig. 2. The charge and mass partition of the asymptotic fragments is obtained from the normalized experimental charge versus mass distribution, $P(Z,A)$, where $P(Z,A)$ is the probability that the fragment has charge Z and mass A. This asymptotic fragment partition will be used to obtain the (earlier time) freeze-out primary fragment partition by removing a few light particles (p, d, t, ^{3}He, and ^{4}He) from the asymptotic fragment partition and absorbing them in to what then become the primary IMF's. The full procedure is described in Appendix B. The freeze-out volume V_{fo} is calculated, as is done by Bondorf *et al.* [24], by including sufficient volume for each fragment to ensure negligible nuclear interaction. The LCP's are uniformly distributed within a prolate spheroidal shape with the unique axis directed along the beam direction. The IMF's are randomly distributed according to two three-dimensional Gaussian distributions. As we shall see, such a selection of the LCP and IMF distributions is consistent with experimental observables (see Fig. 8) as well as dynamical simulations of the early stage of the reaction (for example the CHIMERA calculations).

Figure 4 presents the algorithm used for determining the fragment velocities at freeze-out. The fragment asymptotic kinetic energy in the c.m. system is chosen from the ''true'' asymptotic distribution, and the modulus of velocity is calculated according to $|\mathbf{v}_i| = \sqrt{2E_i^{\text{asym}}/A_i}$. The procedure is iterative, starting with $E_i^{\text{asym}} = E_i^{\text{expt}}$. One procedure (a) has been developed in order to assign a direction to the fragment velocity, based on the assumption that the fragment energy is a sum of the radial and the thermal energies. This procedure is described in Appendix A. Another procedure (b) has been introduced in order to convert the set of ''true'' asymptotic fragment velocities $\{v_i\}$ into the set of the primary fragment velocities $\{\mathbf{v}_i^{\text{fo}}\}$. This backtracking procedure corrects the effects of Coulomb acceleration and collective rotation and it makes use of the relations and algorithms described by Randrup [25]. Needless to say, these quantities, and thus these procedures, are of central importance to this work.

D. Tuning of the model input

In order to obtain the freeze-out configuration, true asymptotic distributions (unmodified by the detection system) have been generated using the self-consistent iterative procedure presented in Fig. 4 and the following experimental observables: (i) the LCP multiplicity distributions, (ii) the IMF multiplicity distribution, (iii) the charge distribution, and (iv) the energy spectra (in c.m. system) for each fragment species. Due to limited acceptance of our detection system in the most forward and backward directions, the

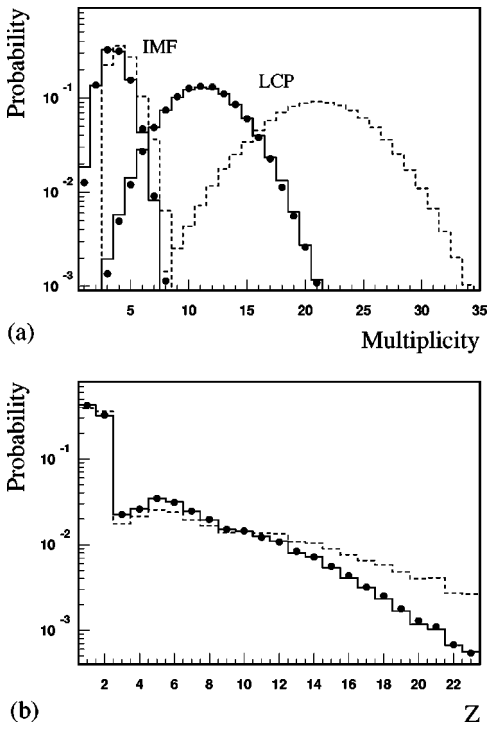

FIG. 5. (a) The LCP and IMF multiplicity distributions and (b) the fragment charge distribution. The solid points show the experimental data, solid-line and dashed-line histograms show filtered and unfiltered (''true'') asymptotic model distributions.

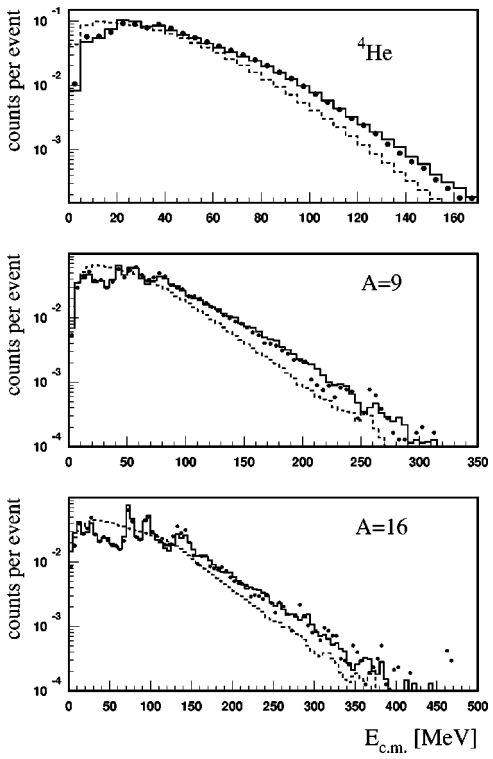

FIG. 6. The experimental energy spectra in the c.m. system (dots). The dashed lines and solid lines represent the ''true'' asymptotic distributions and the distributions when the detector filter has been included, respectively.

experimental observables used in this analysis are only slightly contaminated by preequilibrium particles. This contention is supported by the CHIMERA simulations [19].

The experimental LCP and IMF multiplicity distributions, the fragment charge distribution, and the energy spectra in the c.m. system are represented by solid dots in Figs. 5 and 6 for selected fragment species. The desired true asymptotic distributions are shown in these figures by the dashed-line histograms. When the detector filter is applied to these true distributions, the experimental observables are well reproduced by the model calculation as indicated by the solid-line histograms in Figs. 5 and 6.

The second set of adjusted parameters includes both the shape of the freeze-out volume and the ratio of the average values of the radial proton energy to the total proton kinetic energy, p_p (see Appendix A for details). The spheroidal shape of the freeze-out volume has been parametrized by the ratio c/a, were c and a are the major and minor semiaxes of the spheroid, respectively. We found that the angular distributions in the c.m. system are very sensitive to both the p_p and c/a parameters. Figure 7 presents calculated primary angular distributions for selected species. These histograms represent calculations assuming either a spherical shape of the freeze-out volume ($c/a=1$) and $p_p=0.4$ (dotted), or a nonspherical freeze-out shape $c/a=4$ with no radial energy $p_p=0$ (dashed) and with a substantial radial energy $p_p=0.4$ (solid). The results shown in Fig. 7 were generated without the detector filter while those shown in Fig. 8 were generated using this filter. The latter can be directly compared to the experimental distributions that are represented by solid dots. One can see that the experimental angular distributions for the heavier fragments are reproduced by the model calculation only when the elongated shape of the freeze-out volume is assumed. The LCP angular distributions in particular are sensitive to the p_p parameter, and the best agreement between calculation and the experimental data is for $p_p \approx 0.4$.

It should be noted that our selection criterion is different from that employed in Ref. [26]. The most conspicuous difference is that our criterion does not directly bias against nonspherical event shapes while the selection criteria in Ref. [26] does. Our choice of filters is in fact motivated by this difference in that reaction simulations of central collisions do produce elongated event shapes.

IV. RESULTS

A. Secondary evaporated LCP multiplicities

The reconstruction procedure described above is applied to those events that pass our selection for violent collisions (see Sec. II B). Due to rather modest statistics, the analysis of the primary IMF excitation energy has been done for four element groups, as indicated in Table I, rather than for individual elements.

Similar analyses to those represented in Fig. 3 have been done for each bin of the detected IMF and for each type of the LCP. The results of the background subtraction from the detected total LCP emission [see Fig. 3(c)] have been used to obtain the experimental correlation functions presented in

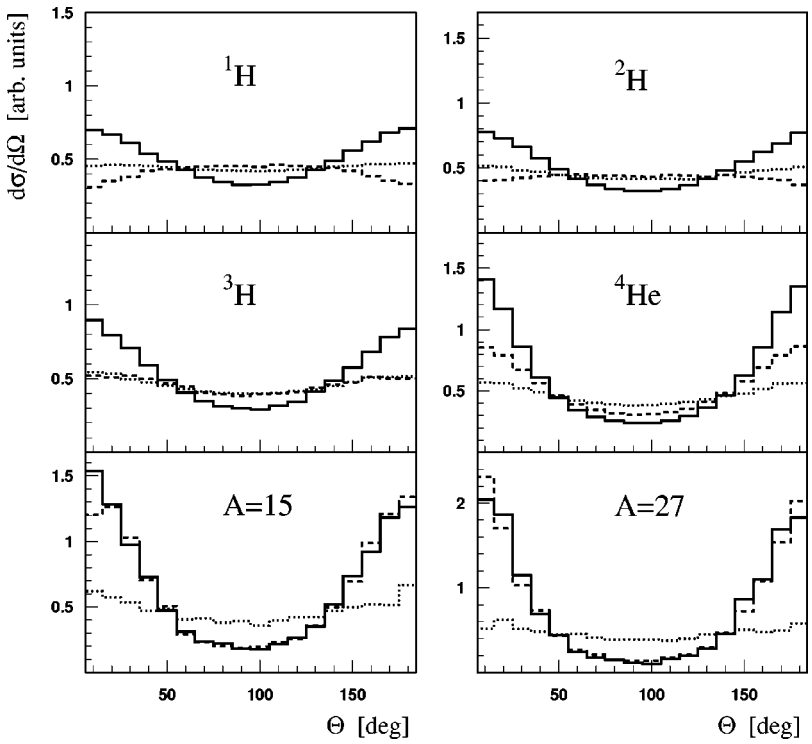

FIG. 7. The angular distributions in the c.m. system for the model calculation (the detection filter has not been included). Dotted histogram, $c/a=1$, $p_p=0.4$; dashed histogram, $c/a=4$, $p_p=0$; and solid histogram, $c/a=4$, $p_p=0.4$ (see text for explanation).

Fig. 9 as solid lines. These correlation functions display the relative energy distributions between the LCP and the daughter IMF defined as

$$E_{\rm rel}=\frac{\mu(v_\perp^2+v_\parallel^2)}{2},$$

where μ is the reduced mass of the IMF-LCP system and $v_\perp$ and $v_\parallel$ were defined in Sec. III A. The IMF masses are those for β-stable nuclei. By performing the additional calculations we found that a variation on the cold fragment masses by ± 1 mass unit has a negligible effect on our final result.

The correlated LCP multiplicities, $M_{\rm expt}(k,j)$ have been varied to reproduce (simultaneously) the experimental correlation functions for five types of LCP's (j modes) and four IMF bins (k bins); see Table I. While a fitting procedure was not done, the variational procedure mentioned above indicates that the multiplicities are well determined. This crude

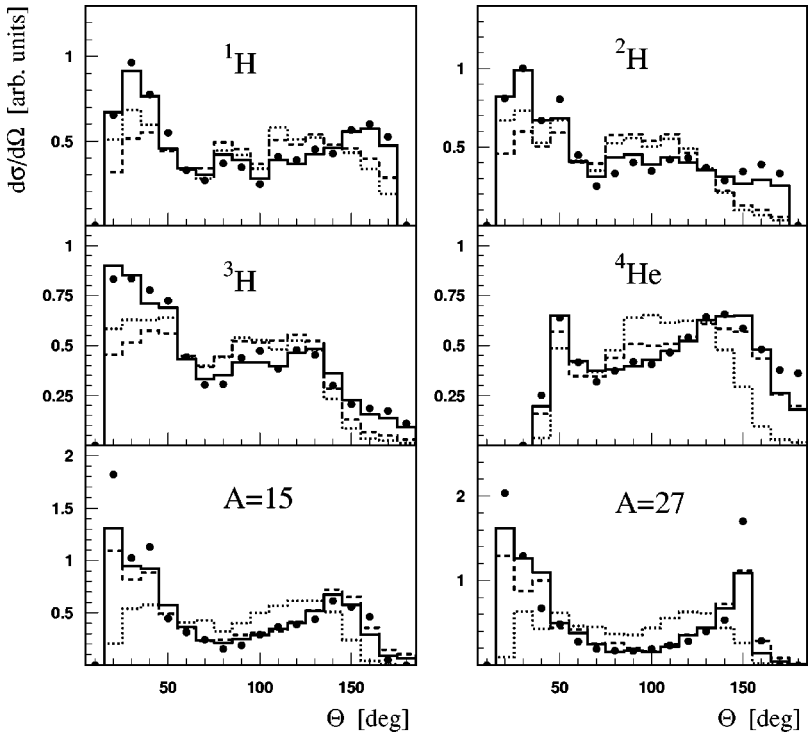

FIG. 8. The angular distributions in the c.m. system for the model calculation. The influence of the detector acceptance has been taken into account. The parameters for the dotted, dashed, and solid histograms are the same as those presented in Fig 7. The experimental data are shown as solid points.

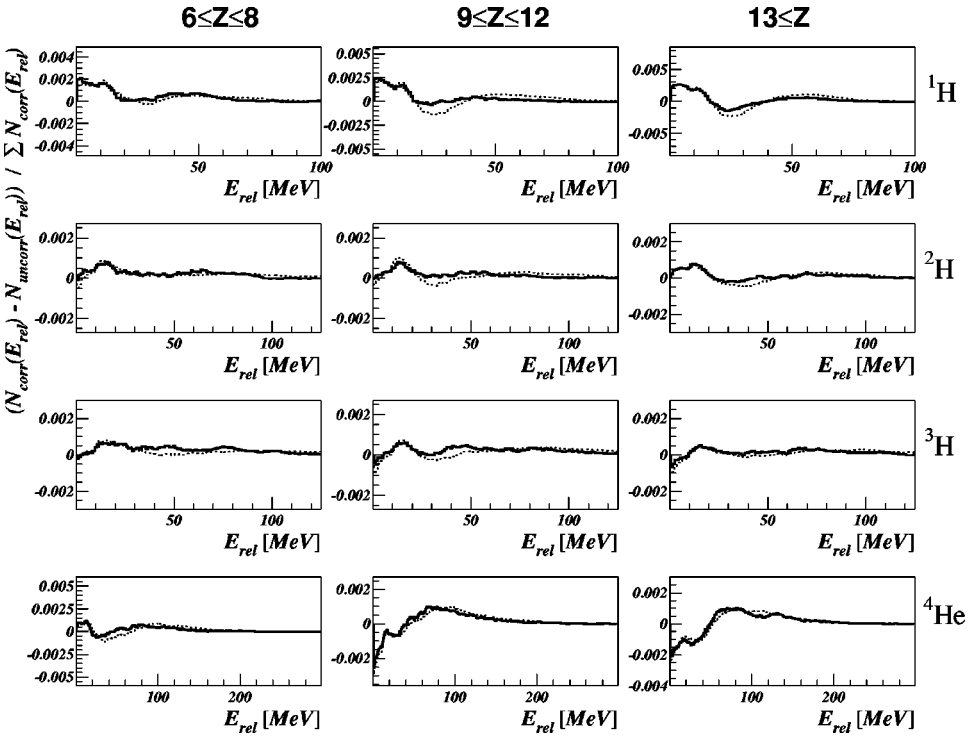

FIG. 9. Net experimental correlation functions (solid lines). The dotted lines are the results of the model calculation assuming $a/c=4$, $p_p=0.4$, and $\tau=50$ fm/c (see text).

optimization procedure leads to the multiplicities given in Table I. We estimate the uncertainties in these multiplicities to be less than $\pm 25\%$ (see below). The calculated correlation functions are displayed in Fig. 9 as dashed lines. The agreement between the experimental correlation functions and those generated using the multiplicities presented in Table I is very good for both protons and α particles and quite satisfactory for the other LCP isotopes for which the statistics are much more limited. Table I shows that the LCP multiplicities increase with increasing charge of the detected IMF. Such an observation suggests that the total excitation energy increases with the charge of the parent nuclei. The multiplicities for protons are higher than those for α particles. The very low ^{3}He multiplicities agree with experimental data [27] and statistical model calculations [22].

Figure 10 shows the multiplicities of LCP's evaporated from the fragments ($M_{\rm evap}$) and the total LCP production ($M_{\rm tot}$) as well as the ratio of these values. One can see that about 20% of the LCP's come from the secondary statistical decay of the primary fragments and that this contribution strongly depends on the type of evaporated species.

TABLE I. Extracted evaporated multiplicities $M_{\rm expt}$ for the four bins in $Z_{\rm IMF}$.

Species		^{1}H	^{2}H	^{3}H	^{3}He	^{4}He
	j mode					
$Z_{\rm IMF}$	k bin	1	2	3	4	5
3–5	1	0.01	0.0	0.01	0.0	0.06
6–8	2	0.13	0.06	0.05	0.0	0.13
9–12	3	0.39	0.12	0.07	0.0	0.11
$\geqslant$13	4	0.91	0.36	0.26	0.09	0.31

The sensitivity of the calculated correlation functions to the LCP multiplicities is shown in Fig. 11. Here we display the correlation functions calculated for the best set of multiplicities (solid line) and those calculated for multiplicities varied by $\pm 25\%$. Our results show that these correlation-

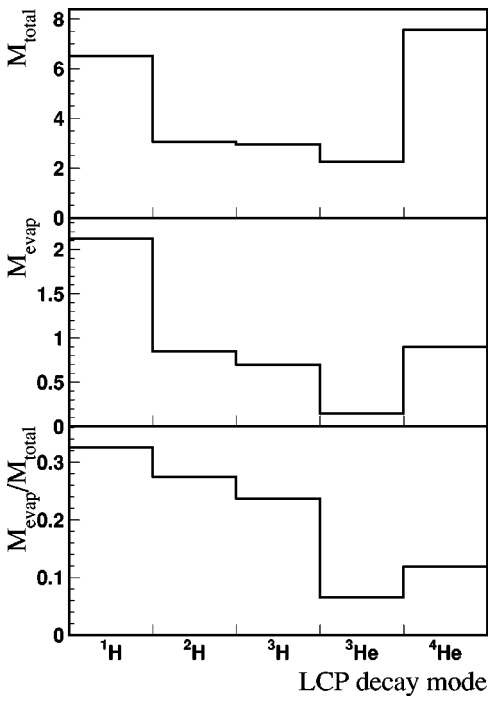

FIG. 10. The total average multiplicities of the LCP (upper panel). The multiplicities of the LCP evaporated by the primary fragments (middle panel) and the ratios of the multiplicities of the LCP evaporated by the primary fragments to the total average multiplicity of the LCP (lower panel).

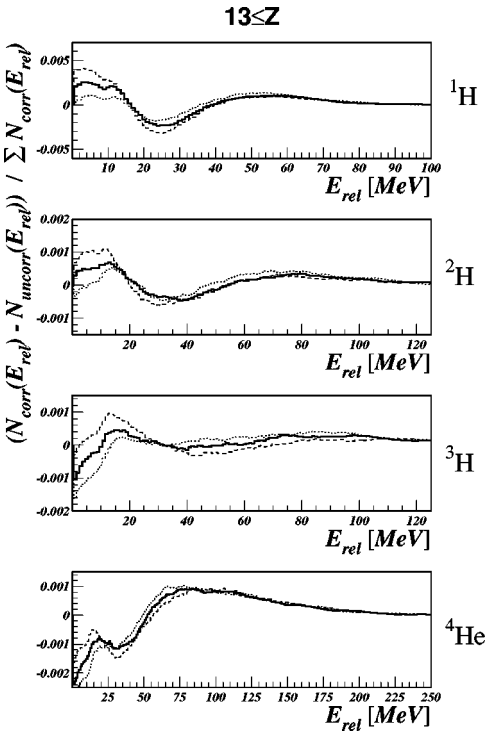

FIG. 11. The correlation functions calculated for the multiplicities, $M_{\mathrm{expt}}(4,j)$ given in Table I (solid lines). Dashed and dotted lines are the calculated correlation functions for 125% and 75% of $M_{\mathrm{expt}}(4,j)$, respectively.

functions do strongly depend on the multiplicity of evaporated LCP's, and therefore these multiplicities can be used for the quantitative extraction of the excitation energies of the primary fragments. The experimental correlation functions always fit within the $\pm 25\%$ corridor, setting the upper limit on the multiplicity uncertainties.

B. Fragment excitation energies and temperatures

In order to convert the LCP multiplicities into the fragment excitation energies, the statistical code GEMINI [22] has been used. The LCP decay from the primary IMF's is treated with the Hauser-Feshbach formalism [28]. The most important parameter of this statistical approach is the level density parameter. In our calculations, three parametrizations have been used:

(I) $a=(A/14.61)(1+4/A^{1/3})$ [29],
(II) $a=(A/13.7)(1+1.3/A^{1/3})$ [30],
(III) $a=(A/13)$ [31,32],

where A is the mass number. These parametrizations and a low-excitation-energy formula ($a=A/8$) are shown in Fig. 12 (upper). Using the relation between the excitation energy and the temperature [33],

$$E^*=aT^2, \tag{2}$$

one can conclude, for constant temperature, that the excitation energy per mass unit is proportional to the ratio a/A. In Fig. 12 (lower) the ratios a/A versus A have been plotted.

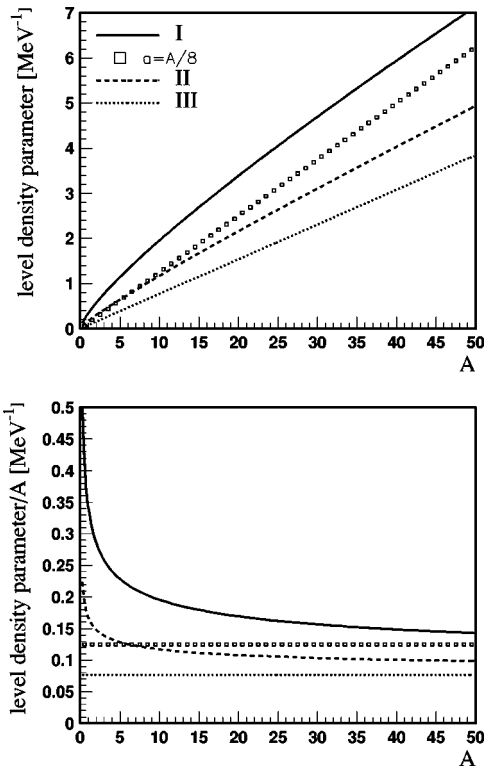

FIG. 12. Level density parameter a (upper panel) and the ratio a/a (lower panel) as the function of the nucleus mass A.

One can see that, at a given temperature, parametrizations (I) and (II) predict higher excitation energies per mass unit for lighter fragments than for heavier fragments. We treat the decaying system at the freeze-out stage as an ensemble at a given temperature where the fragment excitation energies are related to the system temperature by Eq. (2).

As neutrinos have not been detected in the experiment, nor are the masses of the detected IMF's known, an optimization procedure like that used for the charge distribution cannot be employed. Therefore we have investigated two assumptions for the N/Z ratio of the primary fragments. These two assumptions are that the N/Z ratio of the primary fragments is equal to that for β-stable nuclei and that of the combined target-projectile system ($N/Z=1.3$).

The GEMINI calculations supply the average LCP multiplicities $[M_T(k,j)]$ for each LCP type (j mode) in each of the four IMF remnant (k) bins at a given temperature (T). The calculated values of the $M_T(k,j)$ can be directly compared to the values given in Table I. In order to obtain a quantitative comparison between the calculated multiplicities and those derived from the experimental data, the following measure has been used:

$$\chi^2=\sum_{j=1}^{5}\left(\frac{M_T(k,j)-M_{\mathrm{expt}}(k,j)}{M_{\mathrm{expt}}(k,j)}\right)^2\times \mathrm{weight}\,(j), \tag{3}$$

where weight (j) are proportional to the total yields of the selected LCP normalized to the proton yield [weight $(j=1)$ $=1$]. The upper panels in Fig. 13 show the χ^2 parameter as a function of the fragment temperatures calculated for the

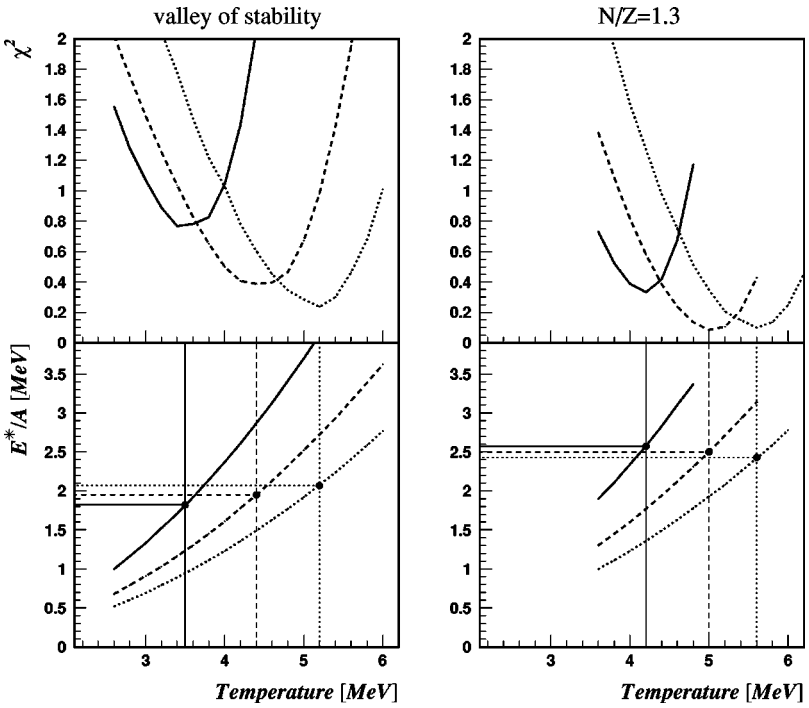

FIG. 13. χ^2 (upper panels) and the fragment excitation energy per nucleon (lower panels) as a function of the temperature. The values of the fragment excitation energies and temperatures at the minimum of the χ^2 are indicated by the horizontal and vertical lines, respectively.

fourth bin ($k=4$) and taking into account the ^{1}H, ^{2}H, ^{3}H, and ^{4}He particle emissions (the ^{3}He has been excluded due to the very low multiplicity of this fragment). The solid, dotted, and dashed lines have been obtained for the level density parametrizations I, II, and III, respectively. The plots presented in the left column were obtained using fragments with β-stable N/Z ratios while the plots in the right column were obtained using fragments with the N/Z ratio of the combined target-projectile system.

The lower panels in Fig. 13 present the average fragment excitation energies per mass unit versus the primary fragment temperature calculated for the three level density parametrizations. The values of the fragment excitation energies and temperatures at the minimum of the χ^2 distribution, marked by dots in the lower panels of Fig. 13, are listed in Table II. The errors included in Table II have been calculated assuming that the LCP multiplicities have been extracted from the experimental data with uncertainties of $\pm 25\%$ (see Fig. 11).

The assumption that the fragment N/Z ratio is the same as in the combined target-projectile system leads to higher fragment excitation energies than does the assumption that the fragment N/Z ratio is the same as for β-stable nuclei. Lower values of the χ^2 (see Fig. 13) arise from the former assumption, indicating that the primary fragments likely reflect the entrance channel N/Z ratio. A similar conclusion was reached in Ref. [23]. This conclusion derives some additional support from the results presented in Fig. 14. Here, the fragment excitation energies per nucleon have been obtained from separate χ^2 minimizations for each evaporated LCP type. In this case also, the assumption that the fragments' N/Z ratio is the same as in the combined target-projectile system leads to more consistent values of the derived excitation energy per nucleon.

Subtracting the evaporated LCP multiplicities from the total LCP multiplicities (see Fig. 12), the primary LCP population at the freeze-out phase is obtained. Using this information the system temperature, $T_{\rm app}=8.85$ MeV, was calculated from the Albergo formula [6]. On the other hand, using the total LCP multiplicities in the Albergo formula one gets $T'_{\rm app}=8.3$ MeV. Clearly the correction for the IMF sequential decay increases of the apparent temperature, in agreement with Refs. [12,9]. Another observation is that the system temperature $T_{\rm app}$ is much higher than those presented in Table II. A similar observation was made in Ref. [14] and explained by differences in the emission environments of ^{3}He as compared to the emission environment of the α par-

TABLE II. Extracted values for both E^*/A and T for the three different prescriptions for the level density parameter and the two assumptions for the N/Z ratio.

	Valley of stability		$N/Z=1.3$	
a	E^*/A (MeV)	T (MeV)	E^*/A (MeV)	T (MeV)
(I)	$1.8^{+0.45}_{-0.32}$	$3.5^{+0.4}_{-0.3}$	$2.57^{+0.38}_{-0.42}$	$4.2^{+0.3}_{-0.4}$
(II)	$1.95^{+0.45}_{-0.35}$	$4.4^{+0.45}_{-0.4}$	$2.5^{+0.4}_{-0.4}$	$5.0^{+0.04}_{-0.4}$
(III)	$2.1^{+0.35}_{-0.45}$	$5.2^{+0.4}_{-0.6}$	$2.43^{+0.37}_{-0.42}$	$5.6^{+0.4}_{-0.5}$

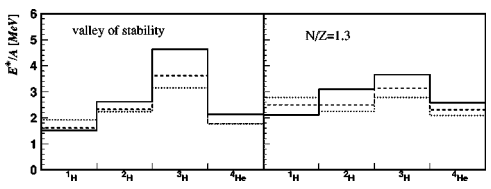

FIG. 14. Fragment excitation energies obtained independently for ^{1}H, ^{2}H, ^{3}H, and ^{4}He particles. Solid, dashed, and dotted lines refer to the level density parametrizations I, II, and III, respectively.

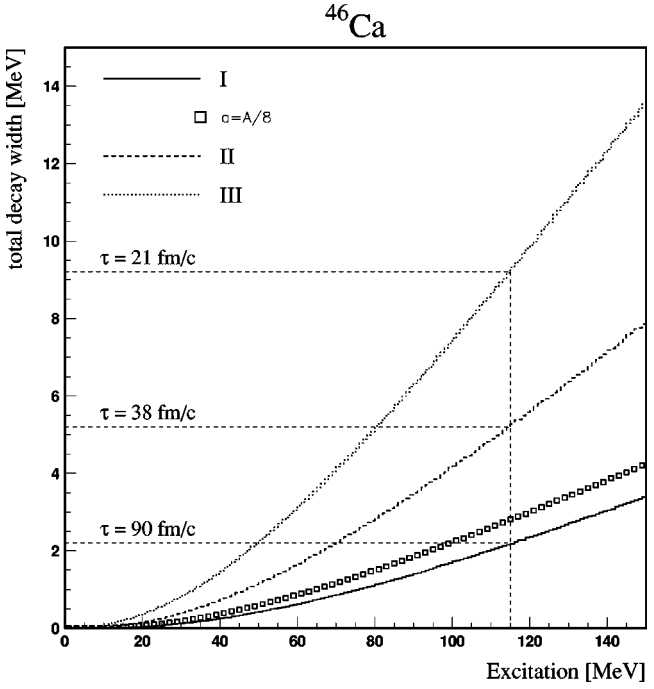

FIG. 15. Total decay width of the ^{46}Ca nucleus as a function of the excitation energy. Indicated values 90, 38, and 21 fm/c refer to the mean lifetime of the ^{46}Ca nucleus at excitation energy 115 MeV for the level density parametrizations I, II, and III, respectively.

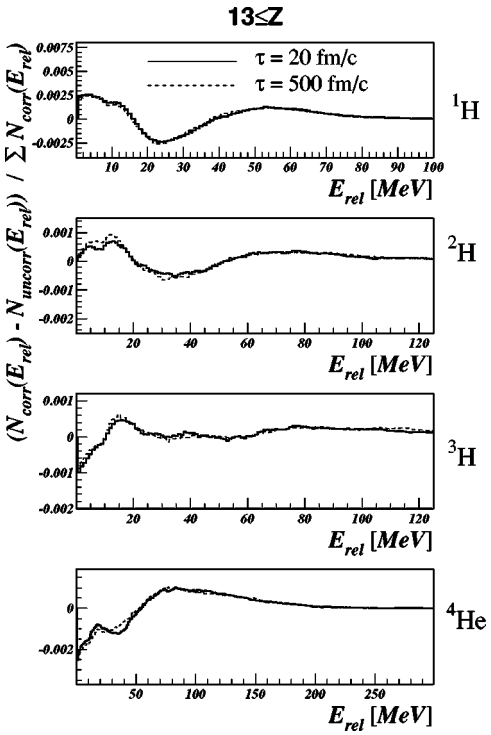

FIG. 16. Correlation functions calculated for $\tau=20$ and 200 fm/c for ^{1,2,3}H and α particles.

ticles due to a hierarchy or ordering of mean emission times. However, as our ^{3}He multiplicities might be slightly inflated by contamination due to an incomplete rejection of ^{4}He, the $T_{\rm app}$ values are subject to a systematic overestimation.

C. Decay time scale

The temperatures of the primary IMF's, which have been presented in the previous section, depend on the level density parametrization used (Table II). The calculated mean lifetime of the excited IMF also depends upon the level density parametrization as seen in Fig. 15. The Hauser-Feshbach formalism has been used [22,28] to calculate the total decay width of a ^{46}Ca nucleus as a function of the excitation energy. The solid, dashed, and dotted lines in Fig. 15 refer to the level density parametrizations I, II, and III, respectively, and the squares represent the low-energy formula ($a=A/8$) (see Sec. IV B). The ^{46}Ca nucleus has been chosen as an example of an IMF with the same N/Z ratio (1.3) as the combined target-projectile system. One can see that the calculated decay time of the excited nucleus is strongly dependent on the level density parametrization. In Fig. 15, the dashed vertical line indicates 115 MeV of excitation energy, which corresponds to the experimentally deduced primary IMF excitation of 2.5 MeV/nucleon. The mean lifetime of the ^{46}Ca nucleus at this excitation energy is 90, 38, and 21 fm/c for the level density parametrizations I, II, and III, respectively.

If the decay of the excited IMF is very fast, the secondary decay can occur in the close proximity to the other fragments. When this happens the emitted LCP interacts with other fragments, via the long-range Coulomb force, which potentially can decorrelate the relative velocity between the primary IMF and its LCP's. The influence of such an effect would yield IMF excitation energies that are systematically low. Figure 16 presents a comparison of the correlation functions calculated for $\tau=20$ fm/c (solid lines) and $\tau=200$ fm/c (dashed lines). The $\tau=20$ fm/c corresponds to very fast deexcitation of the primary IMF's and thus the expanding nuclear system is still close to the freeze-out stage. Even with such a short characteristic decay time, which is that for the largest level density constant (III), the correlations are only slightly different from the correlation functions calculated using the much slower decay. This comparison indicates that the potential decorrelation process mentioned above is negligible and therefore the derived information on the IMF excitation energies and temperature can be related to the freeze-out condition.

V. CONCLUSIONS

The conclusions of this work are the following. (a) For central collisions of $E/A=45$ MeV ^{84}Kr with ^{93}Nb, the excitation energy of primary fragments at freeze-out has been determined to be $\sim$2.5 MeV/nucleon. (b) The assumption that the fragment N/Z ratio is the same as that for the combined target-projectile system leads to higher fragment excitation energies than does the assumption that the fragment N/Z ratio is the same as for β-stable nuclei. The experimental data are better reproduced with a reaction simulation with the former assumption, indicating that the primary IMF's likely reflect the entrance channel N/Z ratio. (c) About 80% of the detected LCP's do not originate from the secondary

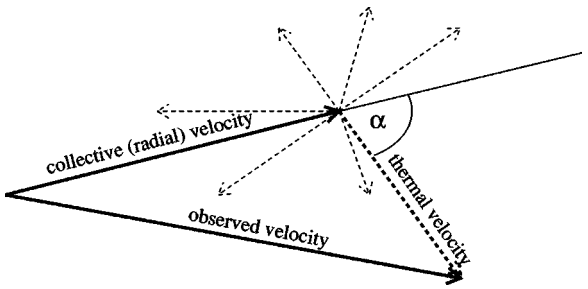

FIG. 17. Fragment velocity decomposition. Dashed arrows represent the thermal fragment velocity distribution. Thick arrows show an example of the total observed velocity construction.

statistical decay of the primary fragments. However, this analysis does not allow us to differentiate those particles that have been produced in the preequilibrium phase of the reaction from those that coexist with the primary IMF's at freeze-out. (d) The temperatures extracted in this work depend on the level density parametrization used in the statistical calculation and thus independent information on the level density parameter is required for an unambiguous fragment temperature determination. (e) The comparisons of the model reaction simulations to the experimental data suggest that the freeze-out volume is extended along the beam direction (nonspherical).

This analysis also enables us to extract information on the partition of energy between the thermalized and collective radial modes. This, and related issues, will be dealt with in a separate paper.

ACKNOWLEDGMENTS

This work was supported by the Polish Scientific Research Committee under Grant No. 2P03B 103 12 and by the Director, Office of High Energy and Nuclear Physics, Nuclear Physics Division of the U.S. Department of Energy under Grant Nos. DE-FG02-87ER40316 and DE-FG02-88ER40406.

APPENDIX A: KINETIC ENERGY COMPONENTS AND RELATED VELOCITIES

The total velocity, $\mathbf{v}(A)$, of the detected fragment of a type A ($A=p$, d, t, ^{3}He, ^{4}He, ^{6}Li, ^{7}Li, . . .) is a result of both a collective motion $\mathbf{v}_R$ and a thermal motion $\mathbf{v}_T$ (see Fig. 17). Now we introduce the assumption that the collective velocity $\mathbf{v}_R$ is proportional to the fragment's position vector $\mathbf{r}$,

$$\mathbf{v}_R=\beta\mathbf{r}, \tag{A1}$$

where β is a scaling factor. Consider the particles positioned at $r\equiv|\mathbf{r}|$. An average value of the square of the total velocity, $\mathbf{v}(A)=\mathbf{v}_R(A)+\mathbf{v}_T(A)$, at the position $\mathbf{r}$, is given by

$$\langle\mathbf{v}^2\rangle=(\beta\mathbf{r})^2+\langle\mathbf{v}_T^2\rangle+2\beta r\langle v_T\cos(\alpha)\rangle, \tag{A2}$$

where α denotes the angle between $\mathbf{v}_R$ and $\mathbf{v}_T$ (see Fig. 17). Due to our assumption that the $\mathbf{v}_T$ has an isotropic distribution the third term on the right-hand side of Eq. (A2) is equal to zero. Multiplying both sides of Eq. (A2) by $m_A/2$, where m_A is the mass of the fragment type A, we obtain

$$\langle E(A,r)\rangle_T=E_R(A,r)+\langle E_T(A,r)\rangle_t. \tag{A3}$$

$\langle E(A,r)\rangle_t$ and $\langle E_T(A,r)\rangle_t$ refer to the average values of the total and the thermal energies, respectively, and $E_R(A,r)$ refers to the collective energy of the particle at position r. Subscript t indicates the averaging over the thermal particle distribution at position r. Introducing an average over the particle position distribution in the freeze-out volume, we obtain

$$\langle E(A)\rangle_{t,r}=\langle E_R(A)\rangle_r+\langle E_T(A)\rangle_t. \tag{A4}$$

The subscript r has been omitted in the last term in Eq. (A4) because the thermal energy is position independent for a system in global thermal equilibrium. Denoting the ratio of the average value of the collective energy to the average value of the total kinetic energy by p and using Eq. (A4), one can obtain

$$\langle E_T(A)\rangle_t=[1-p(A)]\langle E(A)\rangle_{t,r}. \tag{A5}$$

The global thermalization assumption requires that the thermal energy, $\langle E_T\rangle_t$, is equal for all fragments and, e.g.,

$$\langle E_T\rangle_t=(1-p_p)\langle E(p)\rangle_{t,r}, \tag{A6}$$

where $p_p\equiv p$ ($A=$proton). Using Eqs. (A5) and (A6), one can get

$$p(A)=1-\frac{(1-p_{\rm prot})\langle E(p)\rangle_{t,r}}{\langle E(A)\rangle_{t,r}}. \tag{A7}$$

From Eq. (A4) one can calculate the scaling factor

$$\beta=\sqrt{\frac{2(\langle E(A)\rangle_{t,r}-\langle E_T\rangle_t)}{m_A\langle r^2\rangle_r}}=\sqrt{\frac{2p(A)\langle E(A)\rangle_{t,r}}{m_A\langle r^2\rangle_r}}. \tag{A8}$$

This equation shows that the scaling factor in Eq. (A1) is determined by the asymptotically observed fragment energies and by the mean-square radius of the fragment distribution within the freeze-out volume.

Now, we are prepared to follow procedure (a) in Fig. 4. At first, we calculate the freeze-out fragment partition, the fragment positions in the freeze-out volume, and the modulus of each fragment asymptotic velocity (see Sec. III C and Appendix B). Using Eqs. (A8) and (A1) we calculate $\mathbf{v}_{R,i}$ for the ith fragment in the partition, where $i=1,\ldots,M_{\rm tot}^{\rm fo}$. Then, for the ith fragment a set of N thermal components, $\mathbf{v}_{T,i}^l$, are generated, where $l=1,\ldots,N$ (see Fig. 17). The components of the $\mathbf{v}_{T,i}^l$ in the x,y, and z directions are independently chosen from the Gaussian distribution centered at zero with $\sigma=\sqrt{T_i/m_i}$, where

$$T_i=\tfrac{1}{3}m_i\beta^2(A)r_i^2+\tfrac{2}{3}E_i. \tag{A9}$$

E_i and m_i are the total energy and mass of the ith fragment, respectively. The total velocity of the ith fragment is constructed from the radial and thermal components:

$$\mathbf{v}_i^l = \mathbf{v}_{R,i} + \mathbf{v}_{T,i}^l, \quad l = 1, \ldots, N. \tag{A10}$$

Equation (A10) defines a set of N different velocities, $\mathbf{v}_i^l$, for the ith fragment, and the average value of the total ith fragment kinetic energy over l is equal to

$$\langle E_i^l(A)\rangle_l = \tfrac{1}{2} m_i [\beta(A) r_i]^2 + \tfrac{1}{2} m_i \langle (\mathbf{v}_{T,i}^l)^2 \rangle_l . \tag{A11}$$

The last term in the above equation is equal $\frac{3}{2} T_i$ for large N. Using Eq. (A9) we get

$$E_i = \langle E_i^l \rangle_l . \tag{A12}$$

This procedure generates N events with the same fragment partition, initial fragment positions and initial radial velocities. Such events differ in the thermal velocity components.

It is simple to prove that the average kinetic energy of all detected fragments of the type A, $\langle\langle E(A)\rangle_f\rangle_e$, is equal to the average energy of all generated fragments of the same type, $\langle\langle\langle E^l(A)\rangle_l\rangle_f\rangle_e$, where the index f indicates the averaging over all fragments of type A in the event and the index e indicates the averaging over all events. Performing the same averaging over all generated events, we obtain from Eq. (A9)

$$\langle\langle \tfrac{3}{2} T_i(A)\rangle_f\rangle_e = \langle E_T(A)\rangle_t , \tag{A13}$$

where $\langle E_T(A)\rangle_t$ is the average thermal energy derived in Eq. (A5).

APPENDIX B: PRIMARY FRAGMENT PARTITION

In order to generate the primary fragment partition from the asymptotic fragment partition, the decay history of the primary fragments has been traced back. Here, we introduce the following assumptions:

(1) The primary IMF's deexcite by the five-particle modes listed in Table I.

(2) The average multiplicity of the jth deexcitation mode and associated with the IMF remnants of the kth bin are $M(k,j)$ (the bin number definition is given in Table I).

Having $M(k,j)$ one can guess the number of correlated LCP's for each IMF remnant according to the following prescription:

$$M_{\mathrm{eva}}(i,j) = \begin{cases} \mathrm{int}(M(k,j)) + 1 & \text{when } y < M(k,j) - \mathrm{int}(M(k,j)) \\ \mathrm{int}(M(k,j)) & \text{when } y > M(k,j) - \mathrm{int}(M(k,j)), \end{cases} \tag{B1}$$

where y is a random number between 0 and 1, i is the number of the IMF in the fragment partition, and the function $\mathrm{int}(x)$ is defined as the target integer less than x. Now, we can obtain the number of secondary evaporated LCP's,

$$N_{\mathrm{eva}}(j) = \sum_{i=1}^{M_{\mathrm{IMF}}} M_{\mathrm{eva}}(i,j), \tag{B2}$$

where M_{IMF} is the number of IMF's in the partition. The freeze-out fragment partition is constructed by removing $N_{\mathrm{eva}}(j)$ LCP's of the jth mode and by replacing the asymptotic IMF's charges and masses $[Z(i), A(i)]$ with the freeze-out charges and masses $[(Z^{\mathrm{fo}}(i), A^{\mathrm{fo}}(i)]$, using the following equations:

$$Z^{\mathrm{fo}}(i) = Z(i) + \sum_{j=1}^{5} M_{\mathrm{eva}}(i,j) Z_{\mathrm{LCP}}(j), \tag{B3}$$

$$A^{\mathrm{fo}}(i) = A(i) + \sum_{j=1}^{5} M_{\mathrm{eva}}(i,j) A_{\mathrm{LCP}}(j), \tag{B4}$$

where $Z_{\mathrm{LCP}}(j)$ and $A_{\mathrm{LCP}}(j)$ are the charge and mass of the jth mode of the LCP's (see Table I).

[1] L. G. Moretto and G. J. Wozniak, Annu. Rev. Nucl. Part. Sci. **43**, 379 (1993).

[2] D. R. Bowman, G. F. Peaslee, R. T. de Souza, N. Carlin, C. K. Gelbke, W. G. Gong, Y. D. Kim, M. A. Lisa, W. G. Lynch, L. Phair, M. B. Tsang, C. Williams, N. Colonna, K. Hanold, M. A. McMahan, G. J. Wozniak, L. G. Moretto, and W. A. Friedman, Phys. Rev. Lett. **67**, 1527 (1991).

[3] K. Hagel, M. Gonin, R. Wada, J. B. Natowitz, B. H. Sa, Y. Lou, M. Gui, D. Utley, G. Nebbia, D. Fabris, G. Prete, J. Ruiz, D. Drain, B. Chambon, B. Cheynis, D. Guinet, X. C. Hu, A. Demeyer, C. Pastor, A. Giorni, A. Lleres, P. Stassi, J. B. Viano, and P. Gonthier, Phys. Rev. Lett. **68**, 2141 (1992).

[4] R. Wada, D. Fabris, K. Hagel, G. Nebbia, Y. Lou, M. Gonin, J. B. Natowitz, R. Billery, B. Cheynis, A. Demeyer, D. Drain, D. Guinet, C. Pastor, L. Vagneron, K. Zaid, J. Alarja, A. Giorni, D. Heuer, C. Morand, B. Viano, C. Mazur, C. Ngo, S. Leray, R. Lucas, M. Ribrag, and E. Tomasi, Phys. Rev. C **39**, 497 (1989).

[5] T. K. Nayak, T. Murakami, W. G. Lynch, K. Swartz, D. J. Fields, C. K. Gelbke, Y. D. Kim, J. Pochodzalla, M. B. Tsang, H. M. Xu, F. Zhu, and K. Kwiatkowski, Phys. Rev. C **45**, 132 (1992).

[6] K. Albergo, S. Costa, E. Costanzo, and A. Rubbino, Nuovo Cimento A **89**, 1 (1985).

[7] J. Pochodzalla, T. Möhlenkamp, T. Rubehn, A. Schüttauf, A. Wörner, E. Zunde, M. Begemann-Blaich, Th. Blaich, H. Emling, A. Ferrero, C. Gross, G. Immé, I. Iori, G. J. Kunde, W. D. Kunze, V. Lindenstruth, U. Lynen, A. Moroni, W. F. J. Müller, B. Ocker, G. Raciti, H. Sann, C. Schwarz, W. Seidel, V. Serfling, J. Stroth, W. Trautmann, A. Trzcinski, A. Tucholski, G. Verde, and Z. Zwieglinski, Phys. Rev. Lett. **75**, 1040 (1995).

[8] M. L. Tincknell, S. Albergo, F. Bieser, F. P. Brandy, Z. Caccia, D. A. Cebra, A. D. Chacon, J. L. Chance, Y. Choi, S. Costa, J. B. Elliot, M. L. Gilkes, J. A. Hauger, A. S. Hirsch, E. L. Hjort, A. Insolia, M. Justice, D. Keane, J. C. Kintner, V.

Lindenstruth, M. A. Lisa, U. Lynen, H. S. Matis, M. McMahan, C. McParland, W. F. J. Müller, D. L. Olson, M. D. Partlan, N. T. Porile, R. Potenza, G. Rai, J. Rasmussen, H. G. Ritter, J. Romanski, J. L. Romero, G. V. Russo, H. Sann, R. Scharenberg, A. Scott, Y. Shao, B. K. Srivastava, T. J. M. Symons, C. Tuvé, S. Wang, P. Warren, H. H. Wieman, T. Wienold, and K. Wolf, Purdue University report, 1996.

[9] Z. Majka, P. Staszel , J. Cibor, J. B. Natowitz, K. Hagel, J. Li, N. Mdeiwayeh, R. Wada, and Y. Zhao, Phys. Rev. C **55**, 2991 (1997).

[10] K. Kwiatkowski, A. S. Botvina, D. S. Bracken, E. Renshaw Foxford, W. A. Friedman, R. G. Korteling, K. B. Morley, E. C. Pollacco, V. E. Viola, and C. Volant, Phys. Lett. B **423**, 21 (1998).

[11] H. Xi, W. G. Lynch, M. B. Tsang, W. A. Friedman, and D. Durand, Phys. Rev. C **59**, 1567 (1999).

[12] M. B. Tsang, F. Zhu, W. G. Lynch, A. Aranda, D. R. Bowman, R. T. de Souza, C. K. Gelbke, Y. D. Kim, L. Phair, S. Pratt, C. Williams, and H. M. Xu, Phys. Rev. C **53**, R1057 (1996).

[13] V. Serfling, C. Schwarz, R. Bassini, M. Begemann-Blaich, S. Fritz, S. J. Gaff, C. Gross, G. Immé, I. Iori, U. Kleinevoss, G. J. Kunde, W. D. Kunze, U. Lynen, V. Maddalena, M. Mahi, T. Möhlekamp, A. Moroni, W. F. J. Müller, C. Nociforo, B. Ocker, T. Odeh, F. Petruzzelli, J. Pochodzalla, G. Raciti, G. Riccobene, F. P. Romano, A. Saija, M. Schnittker, A. Schüttauf, W. Seidel, C. Sfienti, W. Trautmann, A. Trzcinski, G. Verde, A. Wörner, Hongfei Xi, and B. Zwieglinski, Phys. Rev. Lett. **80**, 3928 (1998).

[14] H. F. Xi, G. J. Kunde, O. Bjarki, C. K. Gelbke, R. C. Lemmon, W. G. Lynch, D. Magestro, R. Popescu, R. Shomin, M. B. Tsang, A. M. Vandermolen, G. D. Westfall, G. Imme, V. Maddalena, C. Nociforo, G. Raciti, G. Riccobene, F. P. Romano, A. Saija, C. Sfienti, S. Fritz, C. Gross, T. Odeh, C. Schwarz, A. Nadasen, D. Sisan, and K. A. G. Rao, Phys. Rev. C **58**, R2636 (1998).

[15] D. W. Stracener, D. G. Sarantites, L. G. Sobotka, J. Elson, J. T. Hood, Z. Majka, V. Abenante, A. Chbihi, and D. C. Hensley, Nucl. Instrum. Methods Phys. Res. A **294**, 485 (1990).

[16] Z. Majka, L. G. Sobotka, D. W. Stracener, D. G. Sarantites, G. Auger, E. Plagnol, Y. Schutz, R. Dayras, J. P. Wieleczko, J. Barreto, and E. Norbeck, in *Nuclear Dynamics and Nuclear Disassembly*, Proceedings of the Symposium, Dallas, Texas, 1989, edited by J. B. Natowitz (World Scientific, Singapore, 1989), p. 424.

[17] M. B. Tsang, Y. D. Kim, N. Carlin, Z. Chen, R. Fox, C. K. Gelbke, W. G. Gong, W. G. Lynch, T. Murakami, T. K. Nayak, R. M. Ronningen, H. M. Xu, F. Zhu, L. Sototka, D. Stracener, D. G. Sarantites, Z. Majka, V. Abenante, and H. Griffin, Phys. Lett. B **220**, 492 (1989).

[18] M. B. Tsang, G. F. Bertsch, W. G. Lynch, and M. Tohyama, Phys. Rev. C **40**, 1685 (1989).

[19] J. Łukasik and Z. Majka, Acta Phys. Pol. A **24**, 1959 (1993).

[20] J. Aichelin, G. Peilert, A. Bohnet, A. Rosenhauer, H. Stöcker, and W. Greiner, Phys. Rev. C **37**, 2451 (1988); G. Peilert, H. Stöcker, W. Greiner, A. Rosenhauer, A. Bohnet, and J. Aichelin, *ibid.* **39**, 1402 (1989); J. Aichelin, Phys. Rep. **202**, 233 (1991).

[21] D. H. Boal and J. N. Glosli, Phys. Rev. C **38**, 1870 (1988); **38**, 2621 (1988).

[22] R. J. Charity, M. McMahan, G. J. Wozniak, R. J. McDonald, L. G. Moretto, D. G. Sarantites, L. G. Sobotka, G. Guarino, A. Pantaleo, L. Fiore, A. Gobbi, and K. D. Hildenbrand, Nucl. Phys. **A483**, 371 (1988).

[23] N. Marie, A. Chbihi, J. B. Natowitz, A. Le Fevre, S. Salou, J. P. Wieleczko, L. Gingras, M. Assenard, G. Auger, Ch. O. Bacri, F. Bocage, B. Borderie, R. Bougault, R. Brou, P. Buchet, J. L. Charvet, J. Cibor, J. Colin, D. Cussol, R. Dayras, A. Demeyer, D. Dore, D. Durand, P. Eudes, J. D. Frankland, E. Galichet, E. Genouin-Duhamel, E. Gerlic, M. Germain, D. Gourio, D. Guinet, K. Hagel, P. Lautesse, J. L. Laville, J. F. Lecolley, T. Lefort, R. Legrain, N. Le Neindre, O. Lopez, M. Louvel, Z. Majka, A. M. Maskay, L. Nalpas, A. D. Nguyen, M. Parlog, J. Péter, E. Plagnol, A. Rahmani, T. Reposeur, M. F. Rivet, E. Rosato, F. Saint-Laurent, J. C. Steckmeyer, M. Stern, G. Tabacaru, B. Tamain, O. Tirel, E. Vient, C. Volant, and R. Wada, Phys. Rev. C **58**, 256 (1998).

[24] J. P. Bondorf, A. S. Botvina, A. S. Iljinov, I. N. Mishustin, and K. Sneppen, Phys. Rep. **257**, 133 (1995).

[25] J. Randrup, Comput. Phys. Commun. **59**, 439 (1990).

[26] N. Marie, R. Laforest, R. Bougault, J. P. Wieleczko, D. Durand, Ch. O. Bacri, J. F. Lecolley, F. Saint-Laurent, G. Auger, J. Benlliure, E. Bisquer, B. Borderie, R. Brou, J. L. Charvet, A. Chbihi, J. Colin, D. Cussol, R. Dayras, E. De Filippo, A. Demeyer, D. Dore, P. Ecomard, P. Eudes, D. Gourio, D. Guinet, P. Lautesse, J. L. Laville, A. Le Fevre, T. Lefort, R. Legrain, O. Lopez, M. Louvel, V. Metivier, L. Nalpas, A. Ouatizerga, M. Parlog, J. Péter, E. Plagnol, A. Rahmani, T. Reposeur, M. F. Rivet, E. Rosato, S. Salou, M. Squalli, J. C. Steckmeyer, B. Tamain, L. Tassan-Got, E. Vient, and C. Volant, Phys. Lett. B **391**, 15 (1997).

[27] S. M. Qaim, C. H. Wu, and R. Wölfle, Nucl. Phys. **A410**, 421 (1983).

[28] W. Hauser and H. Feshbach, Phys. Rev. **87**, 366 (1952).

[29] J. Tõke and W. J. Świątecki, Nucl. Phys. **A372**, 141 (1981).

[30] A. V. Ignatyuk *et al.*, Yad. Fiz. **21**, 1185 (1975) [Sov. J. Nucl. Phys. **21**, 612 (1975)].

[31] M. Gonin, L. Cooke, K. Hagel, Y. Lou, J. B. Natowitz, R. P. Schmitt, B. Srivastava, W. Turmel, H. Utsunomiya, R. Wada, G. Nardelli, G. Nebbia, G. Viesti, R. Zanon, G. Prete, P. Gonthier, and B. Wilkins, Phys. Lett. B **217**, 406 (1989).

[32] M. Gonin, L. Cooke, K. Hagel, Y. Lou, J. B. Natowitz, R. P. Schmitt, S. Schlomo, B. Srivastava, W. Turmel, H. Utsunomiya, R. Wada, G. Nardelli, G. Nebbia, G. Viesti, R. Zanon, B. Fornal, G. Prete, K. Niita, S. Hannuschke, P. Gonthier, and B. Wilkins, Phys. Rev. C **42**, 2125 (1988).

[33] A. Bohr and B. Mottelson, *Nuclear Structure* (Benjamin, New York, 1969), Vol. 1, pp. 183–190.